Part II

Topology-Based Visualization

4 Dynamics of Lagrangian Coherent Structures

The techniques presented in the previous part of this thesis visualize vector fields in an unfiltered way. This can be a drawback for highly complex data sets, especially in three dimensions. In this part, topology-based methods will be applied to filter the data. Therefore, the resulting visualization is reduced by removing unessential parts of the visual representation. In other words, features of data sets are extracted and visualized with the goal of simplifying the analysis of these data sets.

Feature extraction techniques, providing a condensed representation of the essential information, are often applied to the visualization of vector fields. A prominent concept revealing the overall structure is vector field topology [HH89]. Whereas vector field topology is directly applicable only to steady or quasi-stationary vector fields, Lagrangian coherent structures (LCS) [Hal01] are popular for the analysis of time-dependent vector fields. A short introduction to LCS is given in Section 1.5.1.

LCS are a time-dependent counterpart to separatrices, which are stream lines that separate regions of different behavior. LCS have been increasingly subject to research in the last decade and can be obtained as maximizing curves (ridges) in the finite-time Lyapunov exponent (FTLE), a scalar field measuring the separation of trajectories [Hal01]. FTLE computation is, however, an expensive task because at least one trajectory needs to be computed per sample point. LCS behave as material lines under the action of time-dependent flow, i.e., they are advected and exhibit negligible cross-flow for sufficiently long advection time intervals, as reported by Haller [Hal01], Lekien et al. [LCM+05], and Sadlo et al. [SUEW12]. This property gives rise, e.g., to the acceleration technique by Sadlo et al. [SRP11] based on grid advection.

Our approach [BSDW12], that will be detailed in this chapter, adopts the concept of hyperbolic trajectories and space-time streak manifolds. Previous work by Sadlo and Weiskopf [SW10] generalized vector field topology to time-dependent vector fields by replacing the role of stream lines by generalized streak lines [WTS+07]. In this way, critical points turn into degenerate streak lines and separatrices turn into streak lines (space-time streak manifolds) converging toward these degenerate streak lines in forward or reverse time.

Hyperbolic trajectories can be seen as constituent structures in time-dependent 2D vector field topology. As mentioned, space-time streak manifolds—the time-dependent counterpart to separatrices—can be constructed alone from hyperbolic trajectories—no dense sampling is required in contrast to the FTLE approach. However, a major limitation with hyperbolic trajectories is the difficulty of their integration. Although the integration error tends to grow exponentially in linear vector fields, it is usually negligible due to comparably short advection times and low separation rates along common trajectories. Unfortunately, this is not the case in typical hyperbolic configurations due to large separation rates and the fact that both forward and reverse integration are subject to repulsion from one of the LCS (see Figure 4.1).

Hyperbolic trajectories coincide with the intersection of forward and reverse LCS; since ridges in forward FTLE represent repelling LCS whereas those in reverse FTLE are attracting, the trajectory is repelled from the former in forward and from the latter in backward direction. The method presented in this thesis has two advantages: First, avoiding the integration of hyperbolic trajectories by replacing them with intersections of LCS, and second, revealing tangential dynamics in LCS, accomplished by line integral convolution. By treating time as an additional dimension, a stationary visualization is obtained that conveys the overall structure in space-time.

Several approaches for obtaining seeds for hyperbolic trajectories exist: by intersecting ridges in hyperbolicity time [Hal00], ridges in FTLE [SW10], and constructing streak manifolds from them, or by building a time-dependent linear model from critical points [ISW02]. This kind of visualization of hyperbolic trajectories is, however, restricted to LCS geometry, i.e., the dynamics in the vicinity of the hyperbolic trajectories is not conveyed. Furthermore, the hyperbolicity of the vector field is typically analyzed by requiring negative determinant of the velocity gradient. This approach fails in providing insight into the role and importance of hyperbolic trajectories. In contrast, the presented LIC-based visualization captures the configuration of the flow in the neighborhood of hyperbolic trajectories and also in general along LCS. One example is the discrimination of almost parallel flow configurations from strongly hyperbolic ones, as demonstrated in Figure 4.2. This provides increased insight in the overall dynamics, interplay, and importance of LCS, which allows for, e.g., a qualitative analysis of mixing phenomena.

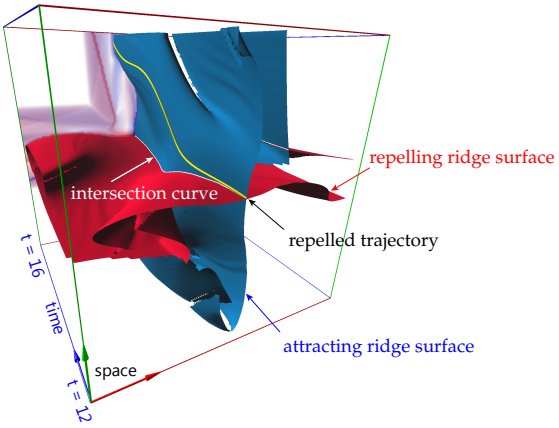

Figure 4.1: Space-time ridge surfaces in forward (red) and reverse (blue) finite-time Lyapunov exponent together with cross section at final time step (colored). The space-time intersection curve in the center (white) represents a hyperbolic trajectory. Traditional integration of the hyperbolic trajectory (yellow curve) from the initial intersection is difficult due to exponential growth of error.

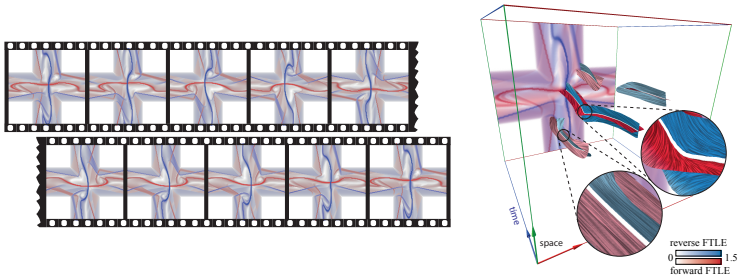

Figure 4.2: Traditional visualization of a time-dependent vector field by time series of the finite-time Lyapunov exponent (left) is difficult to analyze and does not convey the dynamics inside its ridges (LCS). The space-time representation (right) reveals the overall structure and makes the dynamics inside the LCS visible by line texture patterns. Close-ups: in contrast to the traditional 2D visualization, different dynamics along intersection curves (almost parallel flow on the left vs. strongly hyperbolic flow on the right) are apparent.

4.1 Space-Time LCS Visualization

The visualization technique presented in this thesis builds on the fact that time-dependent vector fields can be turned into stationary ones by treating time as additional dimension. This approach is common in the field of differential equations, where non-autonomous systems are made autonomous. Hence, 2D time-dependent vector fields $(u(x,y,t),v(x,y,t))^\top$ are converted into steady 3D vector fields $(u(x,y,t),v(x,y,t),1)^\top$, which are denoted as space-time vector fields. All following steps of the algorithm (see Figure 4.3) take place in this space-time domain. Since 2D path lines represent stream lines in space-time, 3D stream line integration is used over advection time T inside the space-time vector field to generate a flow map $\phi(x,y,t) \mapsto (x',y',t+T)^\top$. Then, for each time slice $\bar{t}$ of the space-time stack, the traditional 2D FTLE is computed according to Haller [Hal01] as

$$1/|T| \ln \sqrt{\lambda_{\max}[(\nabla_2 \phi(x,y,\bar{t}))^\top \nabla_2 \phi(x,y,\bar{t})]},$$

with $\nabla_2 = (\partial/\partial x, \partial/\partial y, 0)^\top$ and major eigenvalue $\lambda_{\max}(\cdot)$. Then, LCS are extracted from the resulting stack of traditional 2D FTLE fields by ridge surface extraction, discussed in Section 4.1.1.

Due to the previously mentioned material advection property of LCS, these surfaces represent stream surfaces in the space-time vector field, i.e., they are tangent to the space-time flow. This allows a direct application of LIC techniques, which is described in Section 4.1.3. By doing this, LIC visualizes the dynamics of path lines along which the LCS are advected, and hence the dynamics within the LCS. As intersections of stream surfaces are stream lines, the space-time intersection of these LCS surfaces from forward and reverse FTLE represents a counterpart to hyperbolic trajectories.

In Section 4.1.2, the investigation of these intersection curves is addressed in terms of hyperbolicity, again based on LCS. Restricting the LIC visualization to bands around the intersection curves helps to avoid occlusion and visual complexity, as shown in Section 4.1.4.

4.1.1 Ridge Surface Extraction

According to Eberly [Ebe96] and following the approach of Sadlo and Peikert [SP09], ridge surfaces are extracted from the stack of 2D FTLE fields as height ridges of co-dimension one from the 3D space-time FTLE field. This approach is used here as well to avoid the problems that would arise from stitching of the individual ridge curves from the 2D FTLE fields. Furthermore, ridges are typically non-manifold, which would cause further issues. Since Eberly's formulation [Ebe96] is local and relies on higher-order derivatives, it

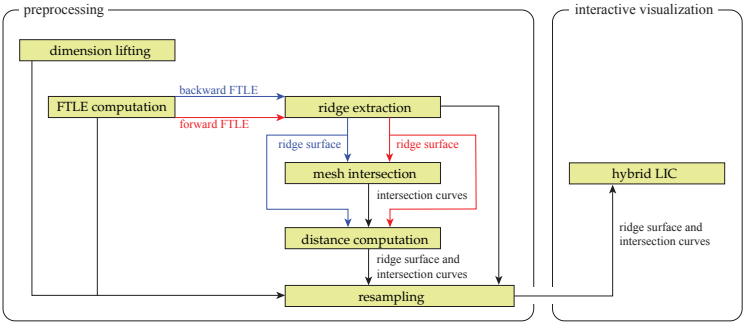

Figure 4.3: Overview of the technique, accompanied by the data that is passed between the stages of the pipeline.

is subject to erroneous solutions. It is therefore common practice to apply filtering. In this thesis, the filtering process described by Sadlo and Peikert [SP07] is applied: since only sufficiently sharp FTLE ridges represent LCS, ridge regions are suppressed where the modulus of the eigenvalue of the Hessian is too low. Further, a minimum FTLE value is required, which is coupled to the minimum separation strength of the LCS. Finally, small ridges are suppressed by filtering ridge surfaces by area. As described by Sadlo and Peikert [SP07], a least-squares approach is used to prevent noise amplification during estimation of the gradient and Hessian. Figure 4.1 shows examples of ridges extracted from a stack of forward and reverse-time FTLE: repelling LCS (ridges in forward FTLE) colored red and attracting ones (ridges in reverse FTLE) blue. The space-time structure of the field is revealed including the intersection curves. However, this does not convey hyperbolicity aspects, e.g., it does not disambiguate intersection curves representing strong hyperbolic trajectories from weak hyperbolic ones. This motivates the visualization of hyperbolicity on LCS as described in the following section.

4.1.2 Visualizing Hyperbolicity

To help the user in the investigation of hyperbolic effects, and hyperbolic trajectories in particular, hyperbolicity is mapped to saturation, as shown in Figure 4.4. The hyperbolicity definition is based on the one by Haller [Hal00]. Haller defines hyperbolicity as the sign of the determinant of the velocity gradient of the original 2D vector field at the respective space-time location. However, in order to obtain a scalar value, the determinant of the velocity gradient is used directly, but only if this value is smaller than zero:

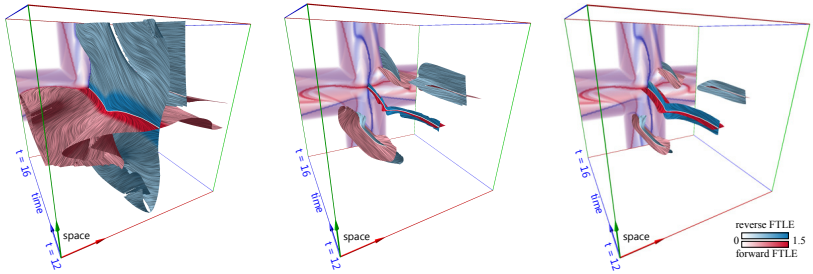

(a) (b) (c)

Figure 4.4: Building blocks for space-time LCS visualization. Advection time for forward and reverse FTLE is $T = 4s$. (a) Space-time LIC qualitatively visualizes LCS dynamics: hyperbolic behavior is apparent. In addition, hyperbolicity is encoded by color saturation. A minimum FTLE value of 0.5 is used. (b) Intersection bands by clipping with complementary FTLE reduce occlusion but still provide context and convey structure of reverse FTLE. The minimum complementary FTLE value is 0.41. (c) Intersection bands by clipping with distance to intersection curves further reduces occlusion and provides the topological skeleton.

$$\text{hyperbolicity} = \begin{cases} 0 & \text{if } \det\nabla u \geq 0 \\ \det\nabla u & \text{else} \end{cases}.$$

One can see how this technique not only reveals the presence of hyperbolicity but also allows for the interpretation of the hyperbolic regions around the intersection curves. To examine hyperbolicity more precisely a novel technique to visualize LCS dynamics is introduced in the next section.

4.1.3 Visualizing LCS Dynamics

The LCS in the space-time FTLE field of this approach are present as ridge surfaces and to fully capture the spatial variation of their dynamics, they lend themselves to dense texture-based visualization such as LIC. Since LCS lack intrinsic surface parametrization and need to be analyzed in overview scales as well as in local detail, image-space oriented approaches are predestined to visualize the space-time structure. The hybrid physical/device-space LIC approach by Weiskopf and Ertl is used here which is detailed in Section 1.4.5.

In the context of this visualization of LCS dynamics, the goal is to visualize the space-time direction of the vector field. Hence, space-time vectors are normalized during LIC computation to obtain LIC line patterns of uniform length for

optimal perception. In contrast to traditional spatial LIC, visual encoding of velocity magnitude is retained in the form of surface orientation in space-time. For example, small angles between surface normal and the time axis indicate high speed.

Figure 4.4a) exemplifies the method again on the same data set. It is apparent how this technique conveys the time-dependent dynamics within LCS. Combining it with the saturation-based visualization of hyperbolicity (Section 4.1.2) supports the identification of hyperbolic intersection curves and still provides the LCS dynamics context. Since LCS are often convoluted, they typically exhibit many intersections that are commonly occluded. This problem is addressed in the next section. At the same time, this approach explicitly addresses the analysis of the intersection curves.

4.1.4 LCS Intersection Bands

Even in the simple example shown so far, it is obvious that occlusion tends to be a problem in space-time visualization of LCS. To address this and to provide a method for analyzing intersection curves of LCS at the same time, two complementary approaches were developed that have proven valuable in experiments, with both approaches restricting the presented visualization to bands around the LCS intersection curves.

As discussed in Section 4.1.1, a common approach is to filter FTLE ridges by prescribing a minimum FTLE value. This way, the visualization is restricted to important LCS, i.e., those representing strong separation. This filter is applied to ridges in both forward and reverse FTLE fields. If an additional minimum value is prescribed for the complementary FTLE, i.e., the reverse in case of forward FTLE ridges and the forward in case of reverse FTLE ridges, one typically restricts the visualization to bands around the intersection curves, shown in Figure 4.4b). This technique has the advantage that the profile of the complementary FTLE field is conveyed, allowing qualitative interpretation of the interplay of LCS. Furthermore, it often features additional bands that do not exhibit LCS intersections. They are generated if FTLE ridges are located in regions of high complementary FTLE. These additional bands are still of interest: the respective regions exhibit both high forward and reverse-time FTLE. Additionally, these bands may connect to other bands that feature intersection curves and hence convey the overall organization of the LCS.

A drawback of this approach, however, is that the bands may get too narrow for appropriate LIC visualization or too wide to sufficiently reduce occlusion. Therefore, an alternative is proposed which restricts LCS to the neighborhood of their intersection curves. First, to avoid numerical issues, regions are omitted where the LCS intersect at small angle. Furthermore, a minimum length of the intersection curves is required to obtain significant visualizations. The remaining intersection curves are then used for distance computation, leading

to a distance field on the LCS that is then used for clipping. Figure 4.4c) shows an example: the dynamics of the LCS is well depicted by LIC and at the same time occlusion is reduced, allowing for the analysis of the intersection curves with respect to LCS dynamics and hyperbolicity. Since the resulting bands can still be too narrow due to perspective foreshortening, depth-corrected width of the bands is supported as described in Section 4.2.2.

To sum up, these clipping approaches result in visualizations that can be seen as an extended topological skeleton of time-dependent flow. Note that equal thresholds are used for forward and reverse-time FTLE ridge filtering as well as for complementary FTLE band clipping, in order to ensure a consistent visualization. Finally, there is a non-disputed similarity to the saddle connectors of Theisel et al. [TWHS03]. However, the approach of this work resides in space-time, whereas saddle connectors visualize 3D steady vector fields.

4.2 Implementation

This section details the implementation of the different building blocks of the technique as well as modifications to existing approaches. The pipeline shown in Figure 4.3 gives an overview of the steps and provides information about the data that are exchanged between different stages of the pipeline.

The software was written in C++. DirectX 9.0 and HLSL for shader programming were used in combination to create the final output images.

4.2.1 Preprocessing

Several steps in this technique are performed in a preprocessing phase. The original data set is given as a series of time steps of a 2D vector field. To create the stationary space-time 3D vector field, dimension lifting is applied, i.e., the time series of the 2D vector field are stacked and the time dimension is treated as additional third dimension. This space-time vector field is used to compute the 3D space-time FTLE field for forward and reverse time direction. Using this FTLE field, ridge surfaces are extracted. A detailed description of the ridge extraction method is given by Sadlo and Peikert [SP07]. The ridge surface meshes from forward and reverse-time FTLE are intersected to obtain the intersection curves. Once the geometry of all intersection curves is obtained, a distance field is computed that holds the distance of ridge surface vertices to the nearest intersection curve.

The next step is to compute vertex-based normals which are used for shading in the interactive visualization. During this process, normals are reoriented if necessary; however, since ridge surfaces are not necessarily orientable, this may not succeed for all normals. Remaining inconsistencies for the normals are treated during interactive visualization using a shader program. Finally, the

space-time flow vectors are sampled at the vertex locations of the ridge surface mesh. This resampling is independent of the FTLE sampling grid, allowing for acceleration methods [GGTH07, SP07, HSW11]. Distance values, normals, resampled flow vectors, and additional scalars like FTLE values, hyperbolicity, and the minor eigenvalue of the Hessian (see Section 4.1.1) are attached to the ridge surface mesh that is then passed to the interactive visualization stage.

4.2.2 Interactive Visualization

The core of this interactive visualization is based on hybrid physical/device-space LIC of Weiskopf and Ertl (see Section 1.4.5) to create line-like texture on the ridge surfaces. During rendering of the space-time ridge surfaces, Phong illumination is applied to enhance visibility and perception of the geometry. Since the ridge surfaces may be non-orientable, local normal vectors must be consistently oriented in order to avoid shading artifacts. Therefore, normal orientation is made consistent during fragment processing using the dot product between the normal and view vector. This prevents inconsistent shading due to normal interpolation; however, ridge surfaces may still appear rippled. This happens because of FTLE aliasing effects at strong and sharp ridges, where very high FTLE gradients are present. To compensate for this, normals are corrected to be perpendicular to the space-time vector field and hence to its LCS during fragment processing.

Occlusion is handled by attaching additional data (regular FTLE, complementary FTLE, and distance to nearest intersection curve) obtained during the preprocessing stage (see Section 4.2.1) to each vertex of the ridge surface mesh. This additional data is then uploaded as texture coordinates to the GPU. Fragments that do not meet the filtering criteria are discarded. All thresholds used in this process are adjustable in real-time by the user. In addition to user controlled clipping, the width of the LCS intersection bands is adjusted based on distance to the camera position. This results in intersection bands with constant image-space width, which reduces occlusion of intersection bands that are close to the camera. At the same time, intersection bands that are farther away are enlarged, which improves visibility of the LIC pattern.

4.3 Results

The presented methods are evaluated by applying them to different data sets. The first two data sets are synthetic, whereas the third is created by CFD simulation, and the fourth is obtained by measurements of ocean currents. The implementation was tested on a PC with an Intel Core Quad CPU (2.4 GHz), 4 GB of RAM and an NVIDIA GeForce 275 GPU with 896 MB of dedicated graphics memory. Each of the presented data sets is visualized at interactive frame rates. The implementation is based on the approach of Weiskopf and Ertl (see

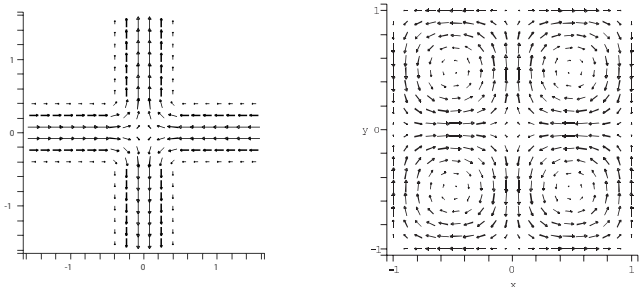

(a) (b)

Figure 4.5: (a) Gyre saddle example at $t = 0$. (b) Quad gyre example at $t = 0$.

Section 1.4.5), therefore, it shows the same performance behavior. Navigation and orientation in space-time is aided by a bounding box of the domain. This bounding box is color-coded—the time dimension is indicated by a blue axis while the two spatial dimensions have a red and green axis, respectively. The last time step of the space-time region of interest is located at the back end of the bounding box which shows the FTLE field as a color-coded texture. In this texture, FTLE values are mapped to saturation, with full saturation mapping to the highest FTLE value. There, the same color-coding is used as for the space-time ridge surfaces.

4.3.1 Oscillating Gyre Saddle

The synthetic vector field used as an example in this section is taken from Sadlo and Weiskopf [SW10]. It exhibits a non-linear saddle shown in Figure 4.5a) that oscillates between the locations $(0.25; 0.25)$ and $(-0.25; -0.25)$ at a period of $\tau = 4$. Resulting visualizations are presented in Figures 4.1, 4.2, and 4.4. To sum up, a strongly hyperbolic intersection curve and several non-hyperbolic ones are visualized in Figure 4.2 (right). This is consistent with the Eulerian picture 4.5a), which shows a distinguished saddle behavior at its center. As mentioned by Sadlo and Weiskopf [SW10], there are other ridges due to shear processes. These are less important for mixing and cannot give rise to hyperbolic trajectories, i.e., their LIC patterns do not show hyperbolic behavior. Please note that FTLE ridges in these examples are filtered to show the strongest and largest LCS only.

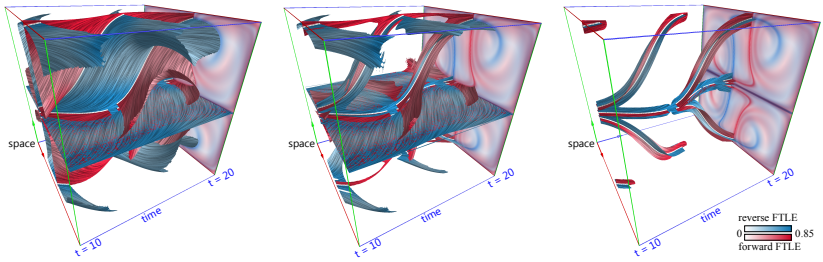

(a) (b) (c)

Figure 4.6: Quad gyre example. The advection time for forward and reverse FTLE is $T = 7.5\,s$. (a) Full visualization of forward and reverse LCS. A minimum FTLE threshold of 0.4 is used. (b) Visualization restricted to complementary FTLE bands. Minor artifacts appear due to aliasing effects of forward and reverse FTLE. The minimum complementary FTLE value is 0.19. (c) Restriction to distance-based LCS intersection bands reveals the topological space-time skeleton.

4.3.2 Quad Gyre

The double gyre example was introduced by Shadden et al. [SLM05] to examine FTLE and LCS, and to compare them to vector field topology. It consists of two vortical regions separated by a straight separatrix that connects two saddle-type critical points: one oscillating horizontally at the upper edge and the other synchronously oscillating horizontally along the lower edge. This is a prominent example where the vector field topology result substantially differs from LCS. This data set is temporally periodic. A larger range of field is used to avoid boundary issues, resulting in four gyres.

As proposed by Shadden et al., the configuration $\epsilon = 1/4$, $\omega = \pi/5$, and $A = 1/10$ is used. Figure 4.5b) shows a plot at $t = 0$ for these parameters. Space-time ridges are heavily occluded when rendering the quad gyre without clipping, as shown in Figure 4.6a). Please note that the $y = 0$ plane represents an LCS in both forward and reverse direction, which results in z-fighting. Nevertheless, the LIC line pattern is consistent in that region due to the image-based LIC technique.

Reducing occlusion by clipping with the complementary FTLE removes parts of the ridge surfaces, while preserving the context of the bands; this is shown in Figure 4.6b). Note, for example, that the red bands are connected at the upper edge of the domain and hence are part of the same LCS. If the space-time ridge surfaces are clipped by distance to their intersection curves, as shown

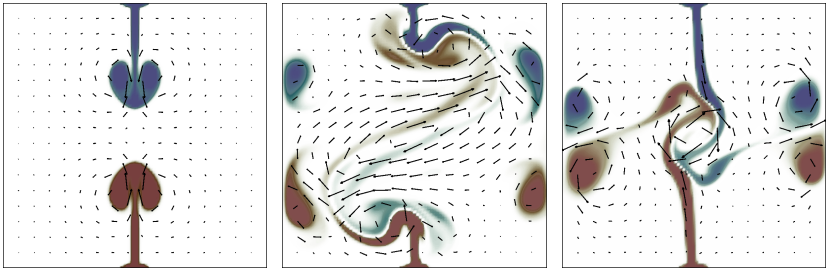

(a) (b) (c)

Figure 4.7: Three time steps of the buoyant plume example, color indicates temperature (red maps to high temperature, blue to low temperature). (a) Two plumes build up and travel toward each other in vertical direction. (b) After collision, two new plumes are created that travel towards the walls. (c) After collision with the side walls.

in Figure 4.6c), occlusion is even more reduced; however, less context is conveyed. Nevertheless, this technique especially pays off for data sets with complex space-time dynamics, since the topological skeleton is well visible from most views. In all images, hyperbolicity is visualized by mapping it to the saturation of the ridge surface color. It can be seen that it readily guides attention to hyperbolic LIC patterns. As in the results by Sadlo and Weiskopf [SW10], a hyperbolic trajectory is identified at the center of the data set.

4.3.3 Buoyant Plumes

The third data set was obtained by a CFD simulation of buoyant 2D flow. A square container was modeled with a small heated region at its bottom wall and a small cooled region at its top wall. Figure 4.7 illustrates the flow. Two plumes develop: a hot one rising to the top and a cold one moving in reverse direction to the bottom. Then, they collide at the center and give rise to two new plumes traveling horizontally toward the side walls. As they approach the walls, they both split and produce plumes traveling in vertical direction. From that point on, the regular behavior is replaced by increasingly turbulent flow behavior. Figure 4.8a) shows the visualization of both forward and reverse-time FTLE ridges. There is no clipping applied for this image, but saturation already guides to the hyperbolic regions, however, many of them are occluded. In Figure 4.8b), the distance-based LCS intersection bands nicely visualize the hyperbolic mechanisms. One can see how the two plumes approach each other and merge, then divide and later give rise to turbulent flow. Finally, several strong hyperbolic regions are identified toward the end of the

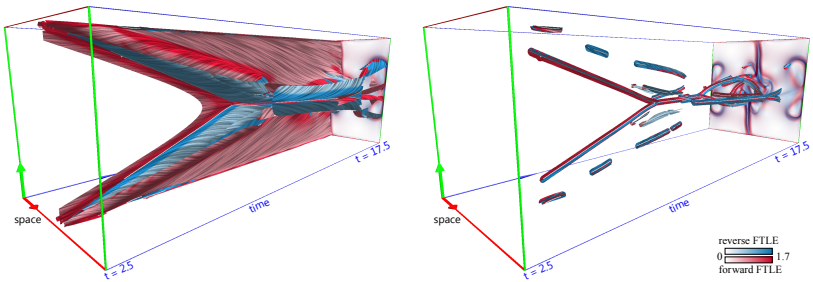

(a) (b)

Figure 4.8: Buoyant plumes example. The advection time for forward and reverse FTLE is $T = 1.5\,s$. (a) Full visualization of forward and reverse LCS. The dynamics of the two plumes is apparent in the first part of the examined time interval. A minimum FTLE threshold of 0.87 is used. (b) LCS intersection bands clipped by distance, revealing the skeleton.

examined time interval. The multitude of hyperbolic regions confirms the observation of strong buoyant mixing. The high intricacy and topological complexity of turbulent buoyant flow is reflected by this visualization.

4.3.4 OSCAR

Ocean Surface Currents Analyses Real-time (OSCAR) [BL02] is a project to calculate ocean surface velocities from satellite data. The OSCAR product is a direct computation of global surface currents using satellite sea surface height, wind, and temperature. The OSCAR analyses have been used extensively in climate studies, such as for ocean heat storage and phytoplankton blooms. The presented technique is applied to the Gulf Stream at the east coast of North America. The focus lies on a strong hyperbolic LCS system involved in mixing, as shown in Figure 4.9a). As expected, the visualization technique reveals a complex Lagrangian skeleton of turbulence [MHP+07]. The LIC patterns allow a direct and qualitative inspection of the LCS with respect to hyperbolic mechanisms and mixing. Whereas many regions in the OSCAR data set exhibited inferior hyperbolic behavior, it is prominent in the selected region. Again, the LCS intersection bands dramatically reduce occlusion while still conveying topological structure and hyperbolic dynamics, as shown in Figure 4.9b).

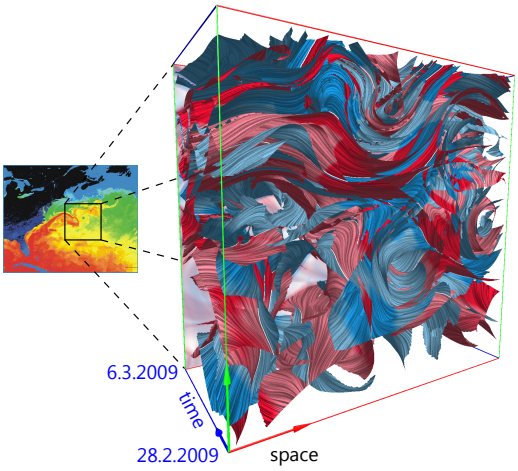

(a)

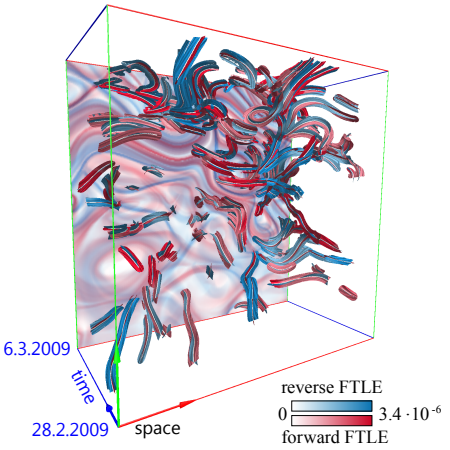

(b)

Figure 4.9: OSCAR example. The advection time for forward and reverse FTLE is $T = 25$ days. (a) Full visualization of forward and reverse LCS. A minimum FTLE threshold of 9×10^{-7} is used. Flow around several intersection curves shows strong hyperbolic behavior. The map shows the Atlantic ocean and the east coast of North America. It gives a frame of reference and exemplifies the prevalent mixing due to the gulf stream. Please note that this map shows water temperature mapped to colors and was generated outside of the investigated time interval. (b) LCS intersection bands clipped by distance.

Following the LIC line patterns along the temporal axis directly conveys the action of the flow in terms of mixing, i.e., thinning and folding.